The Cryosphere Discuss., 9, 3503–3540, 2015
www.the-cryosphere-discuss.net/9/3503/2015/
doi:10.5194/tcd-9-3503-2015

The Cryosphere Discussions
Open Access

Debris-covered energy balance model for Imja-Lhotse Shar Glacier in the Everest region of Nepal

D. R. Rounce[1], D. J. Quincey[2], and D. C. McKinney[1]

[1]Center for Research in Water Resources, University of Texas at Austin, Austin, Texas, USA
[2]School of Geography, University of Leeds, Leeds, LS2 9JT, UK

Received: 02 June 2015 – Accepted: 12 June 2015 – Published: 30 June 2015

Correspondence to: D. R. Rounce (david.rounce@utexas.edu)

Published by Copernicus Publications on behalf of the European Geosciences Union.

Abstract

Debris thickness plays an important role in regulating ablation rates on debris-covered glaciers as well as controlling the likely size and location of supraglacial lakes. Despite its importance, lack of knowledge about debris properties and associated energy fluxes prevents the robust inclusion of the effects of a debris layer into most glacier surface energy balance models. This study combines fieldwork with a debris-covered energy balance model to estimate debris temperatures and ablation rates on Imja-Lhotse Shar glacier located in the Everest region of Nepal. The debris properties that significantly influence the energy balance model are thermal conductivity, albedo, and surface roughness. Fieldwork was conducted to measure thermal conductivity and a method was developed using Structure from Motion to estimate surface roughness. Debris temperatures measured during the 2014 melt season were used to calibrate and validate a debris-covered energy balance model by optimizing the albedo, thermal conductivity, and surface roughness at 10 debris-covered sites. Furthermore, three methods for estimating the latent heat flux were investigated. Model calibration and validation found the three methods had similar performance; however, comparison of modeled and measured ablation rates revealed that assuming a zero latent heat flux may overestimate ablation. Results also suggest that where debris moisture is unknown, measurements of the relative humidity or precipitation may be used to estimate wet debris periods, i.e., the latent heat flux is non-zero. The effect of temporal resolution on the model was also assessed and results showed that both 6 h data and daily average data slightly underestimate debris temperatures and ablation rates, thus these should only be used to estimate rough ablation rates when no other data are available.

TCD
9, 3503–3540, 2015

1 Introduction

Debris-covered glaciers are commonly found in the Everest region of Nepal and have important implications with regard to glacier melt and the development of glacial lakes. It is well understood that a thick layer of debris (i.e., > several cm) insulates the underlying ice, while a thin layer of debris (i.e., < several cm) may enhance ablation (Østrem, 1959; Nakawo and Young, 1981; Nicholson and Benn, 2006; Reid et al., 2012). Spatial variations in debris thickness, particularly where the debris layer thins up-glacier, can also lead to reverse topographic and ablation gradients, glacier stagnation and, ultimately, the development of lakes (Benn et al., 2012). The importance of debris thickness has led many studies to develop models in conjunction with knowledge of the surface temperature to derive debris thickness (Zhang et al., 2011; Foster et al., 2012; Fujita and Sakai, 2014; Rounce and McKinney, 2014). With knowledge of debris thickness, energy balance models may be used to model debris surface temperature, sub-debris ablation rate, and/or runoff downstream (Nicholson and Benn, 2006; Reid et al., 2012; Collier et al., 2014; Fujita and Sakai, 2014). The main factors affecting the performance of these models are the amount of knowledge of the debris properties, the spatial and temporal resolution of the meteorological data, and the assumptions/complexity of the model.

The properties of the debris typically required in debris-covered energy balance models are the albedo, thermal conductivity, and surface roughness. The albedo of debris on glaciers in the Everest region has been found to range from 0.1–0.6 (Inoue and Yoshida, 1980; Kayastha et al., 2000; Nicholson and Benn, 2012; LeJeune et al., 2013). Specifically, Nicholson and Benn (2012) reported that 62 % of measured values ranged between 0.1 and 0.3. Similarly, Kayastha et al. (2000) showed that most values fall between 0.2 and 0.4. The thermal conductivity of debris in the Everest region has been found to range from 0.60 to 1.29 $\mathrm{W\,m^{-1}\,K^{-1}}$ (Conway and Rasmussen, 2000; Nicholson and Benn, 2012; Rounce and McKinney, 2014). The surface roughness, z_0, is arguably the most difficult parameter to measure as it requires an eddy covariance

TCD
9, 3503–3540, 2015

instrument, horizontal wind speed measurements at multiple heights above the surface, or detailed microtopographic measurements (Brock et al., 2006). In the Everest region, Inoue and Yoshida (1980) estimated z_0 to be 0.0035 and 0.060 m for two sites, one consisting of small schist and bare ice and another comprising mainly large granite, respectively. Takeuchi et al. (2000) estimated a similar value of z_0 on the Khumbu glacier of 0.0063 m. On Miage glacier in the Italian Alps, Brock et al. (2010) measured z_0 to be 0.016 m on a debris-covered glacier.

In addition to the properties of the debris, the amount and source of meteorological data available may also greatly influence the model performance. In particular, knowledge related to the latent heat flux on debris-covered glaciers is very limited. This has led previous studies to assume the surface is dry (Foster et al., 2012; Lejeune et al., 2013; Rounce and McKinney, 2014), assume it is dry unless the surface relative humidity was 100 % (Reid and Brock, 2010; Reid et al., 2012; Fyffe et al., 2014), assume a relationship between debris thickness and wetness (Fujita and Sakai, 2014), or use a reservoir approach to model the moisture in the debris (Collier et al., 2014). Collier et al. (2014) suggested that if the atmospheric surface layer is well mixed, then the water vapor pressure between the surface and the air may be assumed to be constant, thereby resulting in a latent heat flux based on the vapor pressure gradient. Fyffe et al. (2014) also commented that the lower portion of the debris near the ice interface was observed to be saturated indicating that there may be evaporation and condensation occurring within the debris, albeit small, even when the surface relative humidity is less than 100 %. The lack of knowledge of the moisture in the debris and at its surface makes it difficult to accurately model the latent heat flux term. These problems are further exacerbated in data scarce regions where automatic weather stations are not available. In these situations, reanalysis datasets must be used for all the required meteorological data (Fujita and Sakai, 2014).

This study develops a method to estimate z_0 using a microtopographic method in conjunction with Structure from Motion (SfM) photogrammetry techniques (Westoby et al., 2012). The z_0 values are used with measured values of thermal conductivity,

TCD
9, 3503–3540, 2015

and previously reported values of albedo to calibrate a debris-covered energy balance model on Imja-Lhotse Shar glacier. Temperature sensors installed at various depths at debris-covered sites were operated from June to October 2014 on Imja-Lhotse Shar glacier and are used for calibration and validation of the model. Various methods for estimating the latent heat flux are investigated. Furthermore, sub-debris ablation rates are compared to ablation stake measurements to assess model performance and the effects of temporal resolution are investigated.

2 Data

2.1 Field data

Field research was conducted on the debris-covered portion of Imja-Lhotse Shar glacier (27.901° N, 86.938° E, ~5050 m a.s.l., Fig. 1) from May to November 2014. Rounce and McKinney (2014) provide a detailed description of Imja-Lhotse Shar glacier so only study-specific details are given here. The field expedition focused on 19 sites on the debris-covered portion of the glacier to determine how debris thickness and topography affect ablation rates. Four sites were used to analyze the surface roughness through the use of SfM and are referred to as Sites A–D (Fig. 2). These sites were selected to represent various grain sizes and mixes of debris that were observed on Imja-Lhotse Shar glacier. Site A was relatively homogenous with the majority of debris being cobble gravel ranging in size from 0.05 to 0.25 m. Site B comprised similar cobbles typically ranging in size from 0.15 to 0.25 m with larger boulders lying on top of the cobble of up to 1.0 m. Site C had the finest debris, which primarily consisted of fines and gravel with some cobbles on the surface up to 0.15 m in size. Lastly, Site D was the most heterogeneous site with boulders ranging up to 0.40 m laying above a surface of cobble of similar size to Site A mixed with the fine and gravel material found in Site C.

Temperature sensors and ablation stakes were installed at 20 other sites; however, data could only be retrieved from 15 of the sites (Table 1). Sites 4–14 were located in

TCD
9, 3503–3540, 2015

a single area that appeared to have developed from differential backwasting over the years. This was the same focus area as described in Rounce and McKinney (2014) and was selected because it appeared to be representative of the debris-covered terrain on Imja-Lhotse Shar glacier and was accessible. Sites 15–20 were located outside of the focus area in an adjacent melt basin to determine if the focus area was representative of other debris-covered areas. At each site, the debris thickness was determined following the methods described in Rounce and McKinney (2014) with the exception of Site 4, where the debris thickness was estimated assuming a linear temperature profile from the mean temperatures over the study period similar to the extrapolation used in Nicholson and Benn (2012). The debris thickness of these sites ranged from 0.07 to greater than 1.0 m. A debris thickness of 1.0 m was considered the maximum due to labor constraints. The slope was also approximated by measuring two points, one 0.5 m uphill from the site and the other 0.5 m downhill, using a total station (Sokkia SET520, ±2.6 mm 100 m^{-1}). The slope at each site ranged from 17 to 37°. The aspect of each site was measured using a compass (Table 1).

Temperature sensors (TR-42 ThermoRecorder, T&D Corporation) were installed and successfully retrieved at 10 sites. These sensors recorded data every half hour from 19 May to 09 November 2014. Each of the 10 sites had a sensor at its surface, which was considered to be installed 1 cm into the debris since debris was placed on top of the sensor. Sites 4, 11, 13, and 14 also had temperature sensors installed within the debris to capture the nonlinear temperature variations in the debris and at three of the four sites the sensors were retrieved such that the thermal conductivity could be estimated.

Ablation stakes were also installed at 14 sites. One site had a debris thickness greater than 1.0 m, so an ablation stake could not be installed. The ablation stakes were installed by excavating to the debris–ice interface, at which point the debris thickness was measured, and then a 2 inch diameter hole was drilled vertically approximately 1.0 m into the ice using a manual ice drill (Kovacs Enterprise). A 2.0 m piece of 11/2 inch PVC pipe was placed into the hole and the height from the top of the ice

TCD
9, 3503–3540, 2015

to the top of the pipe was measured to determine the exact length that the PVC pipe was inserted into the ice. A PVC end cap was then placed on top of the pole to prevent anything from entering the hole through the pipe. The debris was then replaced in its approximate original position.

2.2 Meteorological data

The meteorological data used in the model calibration and validation was from an automatic weather station (AWS), Pyramid Station (27.959° N, 86.813° E, 5035 m a.s.l., SHARE Network operated by EV-K^2-CNR), located 14 km northwest of Imja-Lhotse Shar glacier. The meteorological data provided by Pyramid Station were unvalidated minute measurements of air temperature, wind speed, relative humidity, global radiation, precipitation, and snow depth. The data were processed to be consistent with the half-hour debris temperature measurements on Imja-Lhotse Shar glacier. Wind speed data were collected at 5 m and adjusted to 2 m to be consistent with air temperature measurements for the turbulent heat fluxes assuming a logarithmic dependence (Fujita and Sakai, 2014). The snow depth data were used to derive a snowfall rate. The data were available from 31 May to 12 October 2014 with only a few short gaps. The first two days of meteorological data were used as start-up time for the model. Longwave radiation was not measured at Pyramid Station during this period; therefore, the downward longwave radiation flux from NCEP/NCAR reanalysis data (Kalnay et al., 1996) was used with a minor modification. A comparison of the downward longwave radiation flux from NCEP/NCAR and the incoming longwave radiation flux at Pyramid Station from 2003 to 2010 during the months of June through September revealed that NCEP/NCAR overestimated the incoming longwave radiation by an average of 29 W m^{-2} (results not shown). Therefore, the NCEP/NCAR downward longwave radiation flux was adjusted to account for this overestimation when being used in conjunction with the Pyramid Station data. This reanalysis dataset provides 6 h meteorological data and was resampled using a linear interpolation such that the temporal resolution of the incoming longwave radiation agreed with the half-hour debris temperature measurements.

TCD
9, 3503–3540, 2015

3 Methods

3.1 Surface roughness (z_0)

Structure from Motion (SfM) was used to derive fine-resolution (i.e., centimetric) digital elevation models (DEMs) at four sites (Sites A–D) located on the debris-cover of Imja-Lhotse Shar glacier (Fig. 2). In brief, SfM relies upon the acquisition of a series of overlapping images that capture the features of the terrain from a number of different vantage points. Computer vision techniques detect matching features between images using multiscale image brightness and colour gradients and a highly iterative bundle adjustment procedure is used to develop a three-dimensional structure of the surface (Snavely et al., 2008). Camera positions and orientations are solved simultaneously with surface geometry utilizing the high level of redundancy afforded by a large overlapping image set. Ground control points (GCPs) are then used to transform the relative three-dimensional surface into an absolute coordinate system. The resulting point-cloud data are comparable in both density and accuracy to those generated by terrestrial laser scanning (Westoby et al., 2012) and can either be used as-is, or decimated (as in this study) to generate gridded elevation data. The use of SfM within geoscience is well reviewed by Westoby et al. (2012) and specific details of the mathematical operations involved can be found in Snavely (2008) and Szeliski (2011). Here, we therefore focus mostly on our field method and subsequent roughness analysis.

At each of our sites ~ 40 photos were taken around a roughly 2 m × 2 m grid. Cones were placed in the four corners of the grid as GCPs and their location was measured using a total station with a local coordinate system. The GCPs and photos were processed using Agisoft PhotoScan Professional Edition Version 1.1.0 to create a DEM for each site. At each stage, the highest accuracy settings were chosen. No a priori information about camera position or orientation was recorded, so these were estimated coincidentally as part of the adjustment. In each case the initial estimates of camera position and altitude were accepted and used to generate a sparse point cloud (10^3–10^4 points). A moderate depth filter was then used to derive a dense cloud (10^6–10^7

TCD
9, 3503–3540, 2015

points), and subsequently a mesh was constructed using the height field as the surface type. The resulting DEMs were resampled in ArcGIS 10.3 to a resolution of 0.01 m and were clipped to remove the cones from the subsequent analyses. The DEM was then fit with an x-y plane using a method of least squares such that the DEM was flattened with a mean elevation of zero.

These processed DEMs of the four sites were analyzed to determine the surface roughness, z_0. Lettau (1969) developed an empirical relationship to estimate z_0:

$$z_0 = 0.5 h^* \frac{s}{S} \quad (1)$$

where h^* is the average vertical extent or effective obstacle height, s is the silhouette area or area of the upwind face of an average element, and S is the specific area or unit ground area occupied by each obstacle. Previous studies have estimated the variables in Eq. (1) through a simplified "standard-deviation" approach, which is based on the variations in elevations and the number of continuous positive groups above the mean elevation (Munro, 1989; Rees and Arnold, 2006; Brock et al., 2006). Initially, this standard-deviation approach was applied to measure z_0 for every row and column transect of the four DEMs; however, the resulting values of z_0 did not capture the variations between sites and may have been slightly underestimated (see results).

Consequently, an alternative method was developed to estimate the effective height, silhouette area, and unit ground area of each obstacle using a similar transect approach. Initially, all the relative topographic highs and lows were identified. Any change in elevation greater than 0.01 m was considered a potential obstacle. This was done for all of the transects in each of the four cardinal directions with respect to the DEM, i.e., every East-West, North–South, West–East, and South-North transect. The average height of these potential obstacles was 0.037, 0.055, 0.030, and 0.034 m for Sites A–D, respectively. An obstacle was then defined as any elevation change between a relative low and high that was greater than this average height. The depth of each obstacle was determined as the distance between two low points surrounding the obstacle's high point. In the event that an obstacle was identified, but there was no low

TCD
9, 3503–3540, 2015

point following the high point, i.e., the low point was outside the extent of the transect, then the depth of the obstacle could not be determined. Figure 3 shows an example of a transect from Site B, which identifies the obstacle's height and depth based on the method developed in this study.

The silhouette area and unit ground area were then approximated from the height and depth of the obstacles. Specifically, the silhouette area was taken to be the height of the obstacle times a unit width and the unit ground area was estimated as the depth of the obstacle times a unit width. Based on these definitions, Eq. (1) may be simplified to (Eq. 2):

$$z_0 = 0.5\frac{h^{*2}}{d^*_{\text{obst}}} \tag{2}$$

where d^*_{obst} is the average depth of the obstacle. The surface roughness, z_0, was computed using the average effective obstacle height and average obstacle depth for each transect. In the event that an obstacle was identified, but did not have a depth, the obstacle's height was still used in the average.

3.2 Debris-covered energy balance model

The model used in this study was a steady-state surface energy balance model for a debris-covered glacier, where:

$$R_{\text{n}}(T_{\text{s}}) + H(T_{\text{s}}) + \text{LE}(T_{\text{s}}) + P(T_{\text{s}}) + Q_{\text{c}}(T_{\text{s}}) = 0 \tag{3}$$

where R_{n} is the net radiation flux, H is the sensible heat flux, LE is the latent heat flux, P is the heat flux supplied by rain, and Q_{c} is the ground heat flux (all in W m^{-2}). The net radiation and sensible heat fluxes are fully described in Rounce and McKinney (2014); however, in the current study the incoming shortwave radiation was only corrected for the effects of topography as shading could not be considered due to the lack of a high resolution DEM of the glacier.

TCD
9, 3503–3540, 2015

The latent heat flux is difficult to determine without detailed knowledge of the moisture in the debris or the relative humidity at the surface. As the surface relative humidity was unknown, this study has analyzed three methods for estimating the latent heat flux: (1) assuming the debris is dry (LE = 0), (2) assuming it is dry unless the relative humidity is 100 %, based on the assumption that the water vapor above the surface is well mixed, and (3) assuming the surface is saturated when it is raining. These methods for modeling the latent heat flux will be referred to herein as LE_{Dry}, $LE_{RH_{100}}$, and LE_{Rain}, respectively. The reservoir-approach detailed by Collier et al. (2014) and the empirical relationship between debris thickness and wetness (Fujita and Sakai, 2014) were not applied to this study due to the limited amount of knowledge of moisture within the debris and how the debris properties change with respect to depth. The latent heat flux is thus estimated according to Nicholson and Benn (2006):

$$LE = \left(\frac{0.622\rho_{air}}{P_0}\right) L_e A u (e_z - e_s) \quad (4)$$

where

$$A = \frac{k_{vk}^2}{\ln\left(\frac{z}{z_0}\right)\ln\left(\frac{z}{z_0}\right)} \quad (5)$$

where ρ_{air} is the density of air at standard sea-level pressure ($1.29\,kg\,m^{-3}$), P_0 is the standard air pressure at sea level (1.013×10^5 Pa), L_e is the latent heat of evaporation of water ($2.49\times10^6\,J\,kg^{-1}$), A is a dimensionless transfer coefficient, u is the wind speed at a height of 2 m ($m\,s^{-1}$), e_z and e_s are the vapor pressures (Pa) at height z_0, 2 m, and on the surface of the debris, respectively, k_{vk} is von Karman's constant (0.41), and z_0 is the surface roughness.

The heat flux due to precipitation was estimated following Reid and Brock (2010):

$$P = \rho_w c_w w (T_r - T_s) \quad (6)$$

TCD
9, 3503–3540, 2015

where ρ_w is the density of water (999.97 kg m^{-3}), c_w is the specific heat capacity of water (4.18×10^3 J kg^{-1} K^{-1}), w is the rainfall rate (m s^{-1}), and T_r is the temperature of rain (K), which was assumed to be equal to the air temperature.

The debris layer was broken down into layers of 0.01 m such that the nonlinear temperature profiles in the debris could be captured using a Crank–Nicholson Scheme (Reid and Brock, 2010). The conductive heat flux at the surface and at the debris / ice interface were estimated following Reid and Brock (2010):

$$Q_{c,S} = k_{eff} \frac{T_d(1) - T_S}{h} \quad (7)$$

$$Q_{c,ice} = k_{eff} \frac{T_d(N-1) - T_{ice}}{h} \quad (8)$$

where k_{eff} is the effective thermal conductivity (W m^{-1} K^{-1}), h is the height of each layer in the debris set at 0.01 m, and $T_d(1)$, $T_d(N-1)$, T_{ice} are the temperatures (K) of the first layer in the debris, the last layer before the debris/ice interface, and the temperature of the ice (273.15 K), respectively.

The surface temperature was computed at half-hour time steps using an iterative Newton–Raphson method approach as detailed in Reid and Brock (2010). In the event of snow, a simple snowmelt model was applied (Fujita and Sakai, 2014). The thermal conductivity of snow was assumed to be 0.10 W m^{-1} K^{-1} (Sturm et al., 1997, 2002) and the surface roughness of the snow was assumed to be 0.002 m (Brock et al., 2006). If snow was on the surface, all the heat fluxes at the debris surface were assumed to be zero with the exception of the conductive heat flux in the debris and at the debris/snow interface. If all the snow was melted on the surface, then the next time step returned to the snow-free energy balance model.

As detailed knowledge of albedo, thermal conductivity, and surface roughness was not available for the sites where temperature sensors were installed, the debris-covered energy balance model was calibrated at each site from 02 June to 30 July 2014. The calibration was performed by minimizing the total sum of squares of measured vs.

TCD
9, 3503–3540, 2015

modeled temperatures for each site and was done independently for the three methods used to estimate the latent heat flux. Bounds for the thermal conductivity and surface roughness were based on measured field data (see results), while bounds for the albedo were 0.1–0.4 (Inoue and Yoshida, 1980; Kayastha et al., 2000; Nicholson and Benn, 2012; LeJeune et al., 2013). A validation was then conducted at each site using data from 08 August to 12 October 2014 to assess how well the calibrated model performed.

4 Field results

4.1 Thermal conductivity (k)

The thermal conductivity, k, of the debris was computed using the temperature measurements from Sites 4, 11, and 13 over the time period of the study (02 June–12 October 2014) following the methods of Conway and Rasmussen (2000). The calculations used standard values for the density of rock (2700 $\mathrm{kg\,m^{-3}}$), volumetric heat capacity of rock (750 $\mathrm{J\,kg^{-1}\,K^{-1}}$ ±10 %), and effective porosity (0.33) based on Nicholson and Benn (2012). Depending on the vertical spacing of temperature sensors at a site, k was computed at depths of 0.05, 0.10, and 0.20 m. The values of thermal conductivity ranged from 0.42 (±0.04) to 2.28 (±0.23) $\mathrm{W\,m^{-1}\,K^{-1}}$. The average value of k for each site was 1.44 (±0.14), 1.62 (±0.16), and 0.47 (±0.04) $\mathrm{W\,m^{-1}\,K^{-1}}$ for Sites 4, 11, and 13, respectively. These values agree well with other studies in the Everest region that have found the thermal conductivity to vary between 0.60 to 1.29 $\mathrm{W\,m^{-1}\,K^{-1}}$ (Conway and Rasmussen, 2000; Nicholson and Benn, 2012; Rounce and McKinney, 2014). In September 2014, Rounce and McKinney (2014) found the thermal conductivity to be greatly influenced by depth; however, this trend was not apparent in our current data. We believe this disparity can be explained by the time period during which the data were collected; it is likely that the temporally-limited data presented in Rounce and McKinney (2014) represent a constantly dry surface, whereas here we observed an

TCD
9, 3503–3540, 2015

entire melt season, where the surface is exposed to precipitation and snow. We therefore assume that the effective thermal conductivity does not vary with depth. As k_{eff} is one of the parameters that is used to calibrate the model, the range of average thermal conductivity (0.47–1.62 $W m^{-1} K^{-1}$) is used to bound k_{eff} and at Sites 4, 11, and 13 their average k_{eff} values are used, thereby eliminating one parameter in the calibration.

4.2 Surface roughness (z_0)

The DEMs generated using the SfM workflow had a total root mean square error of 0.008–0.024 m. Table 2 shows that the errors in elevation (i.e., z_0) were smaller than in planform (i.e., x and y) with a maximum error of 0.007 m. The contrast between elevation and planimetric errors is likely because of the identification of the GCPs in each photo during the SfM workflow, since it was easier to identify the top of the cone in each photo than it was to determine the exact point on the rim of the cone. As the error with the total station is small (maximum of 0.4 mm), this human error likely dominated the total error, although errors in estimates of both camera position and orientation, as well as the sparse coverage of GCPs in our plots, will also have contributed. The DEMs were resampled to a resolution of 0.01 m since this was approximately the average error in the x and y directions.

Initially, each DEM was de-trended to account for local slope and z_0 was estimated from Eq. (1) using the standard-deviation approach. The average value of z_0 was 0.0037, 0.0091, 0.0022, and 0.0033 m for Sites A, B, C, and D, respectively. These values are towards the lower end of those previously reported in literature, which range from 0.0035 to 0.060 m (Inoue and Yoshida, 1980; Takeuchi et al., 2000; Brock et al., 2010). In particular, Site B, which comprised large boulders up to 1.0 m in size lying on top of cobble, appeared to be similar to the description of a site on the Khumbu glacier, which had a z_0 of 0.060 m (Inoue and Yoshida, 1980). This further supports the notion that these values of z_0 are likely underestimated, which led to the development of an alternative method.

TCD
9, 3503–3540, 2015

The modified method used in this study takes advantage of the high resolution DEM such that the values of effective height, silhouette area, and unit ground area for each obstacle in a given transect may be estimated. Table 2 shows that using this modified approach the average value of z_0 ranged from 0.007 to 0.030 m. These results agree well with those previously published (Inoue and Yoshida, 1980; Takeuchi et al., 2000; Brock et al., 2010) and appear to capture the variations between sites. Site B had the highest average value of z_0, which was expected since the debris cover includes larger boulders up to 1 m in size (Fig. 2). Furthermore, this value of 0.030 m is similar to the higher value of 0.060 m for z_0 derived from a region on the Khumbu glacier that consisted of large granitic boulders of 1–2 m in size lying on top of schistose rocks with a grain size varying from a few centimeters to 0.5 m (Inoue and Yoshida, 1980). Site C, which comprised the smallest grain sizes of the four sites in this study, agrees well with the smaller value of z_0 (0.0035 m) derived by Inoue and Yoshida (1980) for an area where the supraglacial debris was deposited as dispersed boulders ranging in size of 0.01–0.05 m. The few boulders ranging in size of up to 0.15 m may be the reason for Site C's slightly larger value of z_0 (0.007 m).

Sites A and D were composed of boulders and grains that varied in size between those found in Sites B and C; therefore, we deem the average value of z_0 of 0.011 m for both sites to be reasonable. Despite Sites A and D having the same average value of z_0, the standard deviation of Site D is twice that of Site A (Table 2). The differences in standard deviation appear to capture the relatively homogenous nature of Site A compared to the heterogeneous nature of Site D. Furthermore, Site B, which has the largest variations in terms of grain sizes, also had the largest standard deviation, which would be expected given its surface characteristics.

Typically, z_0 is determined with respect to the direction of the wind. It may be reasonable to assume that the direction of the wind would be up-glacier during the day and down-glacier at night. However, the analysis of z_0 using all 4 cardinal directions with respect to the DEMs showed no apparent trends (results not shown). Therefore, we suggest that averaging the values from all directions yields a good estimate of z_0

TCD
9, 3503–3540, 2015

irrespective of the wind. The range of average z_0 values (0.007–0.030 m) is used to bound z_0 in the model calibration.

4.3 Ablation stakes

Ablation stakes were installed in May 2014 approximately 1 m into the ice at 14 sites with debris thicknesses ranging from 0.07 to 0.54 m (Table 1). The ablation stakes were measured in November 2014. At 11 of the 14 sites, the ablation stakes completely melted out of the ice indicating there was greater than 1 m of ablation. Sites 8, 13, and 15, had ablation measurements of 0.92, 0.85, and 0.89 m, respectively. These three sites had debris thicknesses of 0.20, 0.33, and 0.37 m and were oriented in the southern, northeast, and northwest directions, respectively. The lower ablation rates of Sites 13 and 15 compared to the other 12 sites is likely due to a combination of debris thickness and aspect as they are oriented in a manner that receives less solar radiation throughout the day. Site 8 appears to be an anomaly as it has a smaller debris thickness than 8 of the sites with ablation stakes and a southerly aspect, which positions it in a manner to receive a greater amount of solar radiation throughout the day. It is possible that Site 8 had a higher albedo and/or a lower thermal conductivity, which would greatly reduce its ablation; unfortunately, these properties could not be measured in the field. Nevertheless, the ablation measurements indicate that understanding ablation rates on debris-covered glaciers is greatly influenced by slope, aspect, and properties of the debris (albedo, thermal conductivity, and surface roughness).

5 Modeled results

5.1 Model calibration

Three different methods were used to estimate the latent heat flux to determine how well each method models the measured field data. These methods are referred to as LE_{Rain}, $LE_{RH_{100}}$, and LE_{Dry}. The albedo, thermal conductivity, and surface roughness for

TCD
9, 3503–3540, 2015

each of the three methods was optimized by minimizing the total sum of squares (Table 3). All three methods yielded reasonable values of each parameter when compared to previous work. The albedo values ranged from 0.10–0.40 and had an average value around 0.29, which is consistent with albedos measured in the Khumbu (Inoue and Yoshida, 1980; Kayastha et al., 2000; Nicholson and Benn, 2012; LeJeune et al., 2013). The average value of thermal conductivity was around 1.36 $W m^{-1} K^{-1}$, which is slightly higher than those observed in the Khumbu (Conway and Rasmussen, 2000; Nicholson and Benn, 2012). Lastly, the values of z_0 had an average around 0.020 m, which is consistent with z_0 measured on other debris-covered glaciers (Inoue and Yoshida, 1980; Takeuchi et al., 2000; Brock et al., 2010).

The performance of each model was assessed using the total sum of squares and the R^2 correlation coefficients. The R^2 values ranged from 0.29 to 0.92 for all three models with the exception of Site 13's temperature sensor at 0.20 m, which had an R^2 of around 0.01 for all three models. We suggest that the poor performance at this depth may be because the sensor shifted in the debris over the melt season. A comparison between the modeled and measured daily averages shows the modeled temperatures overestimate the measured temperatures by an average of 1.5 K. This overestimation suggests that the measured temperatures were at a lower depth than the modeled temperatures. Alternatively, the poor performance may be a result of the model calibration, which was performed by minimizing the sum of squares. The difference between the modeled and measured temperatures at lower depths is small compared to variations at the surface. Figure 4c shows that differences between the modeled and measured surface temperatures can be as high as 10 K, so these differences at the surface would affect the calibration to a greater extent than those within the debris. Regardless, we exclude this particular temperature sensor from our subsequent analyses to avoid skewing the results.

The average R^2 values over the calibration period for the LE_{Rain}, $LE_{RH_{100}}$, and LE_{Dry} models were 0.72, 0.72, and 0.69, respectively. Figure 4c and d shows the correlation between the modeled and measured surface temperature at Site 11, which had an

TCD
9, 3503–3540, 2015

R^2 of 0.75 and 0.74 for the calibration and validation periods, respectively. Figure 4c shows there is good agreement between the modeled and measured temperature sensors. The modeled temperatures appear to capture the daily variations in temperature well. However, there are a few days where the nightly low and daily high are overestimated in the model (see for example 6/16–6/18 and 7/25–7/27). Interestingly, the overestimation of the daily high typically occurs after the nightly low was overestimated during the previous night. One possible explanation for these overestimations of the nightly high is an overestimation of the incoming longwave radiation due to the poor temporal and spatial resolution of the NCEP/NCAR reanalysis dataset compared to the other meteorological data from Pyramid Station. Typically, the wind speed during the night is relatively low thereby limiting the turbulent heat fluxes, which causes the incoming longwave radiation to be a major source of energy during this time.

Nonetheless, the model performs well for 19 of the 20 temperature sensors. Unfortunately, it is difficult to determine which latent heat flux model performs the best using the total sum of squares and/or the R^2 values as there was not one particular model that consistently had a lower total sum of squares and/or a higher R^2 at each site. The average R^2 was slightly higher for the LE_{Rain} followed by the $LE_{RH_{100}}$ model, and then the LE_{Zero} model. The total sum of squares of all the sites was also lowest for the LE_{Rain} model followed by the $LE_{RH_{100}}$ model and then the LE_{Zero} model, but the difference between models was less than 6 %. The lack of a single model clearly outperforming the others indicates that either (a) the modeling of the latent heat flux is insignificant or (b) the latent heat flux is significant, but the calibration procedure allows for changes in the latent heat flux to be compensated for via other model parameters.

Brock et al. (2010) found that latent heat fluxes may be a significant energy sink when rain falls on warm debris indicating that the latent heat flux is important to include. They also assessed the importance of each component of the energy balance and found that inclusion of the latent heat flux improved the correlation coefficient of their model. The average latent heat flux for both the LE_{Rain} and $LE_{RH_{100}}$ models were comparable with values ranging from -58 to $8\,W\,m^{-2}$ over the day. The peak instantaneous latent

TCD
9, 3503–3540, 2015

heat fluxes varied greatly between the two models with fluxes as high as −848 and −408 $W m^{-2}$, for the LE_{Rain} and $LE_{RH_{100}}$ models, respectively. These values are similar to those reported by Brock et al. (2010) and support the importance of including the latent heat flux term. However, they do not yield any insight into preference between the LE_{Rain} or $LE_{RH_{100}}$ models.

5.2 Model validation

Model validation was assessed from 08 August to 12 October 2014 for all three models using the R^2 values for each temperature sensor. Excluding the temperature sensor at 0.20 m at Site 13, the R^2 values for the 10 sites ranged from 0.40 to 0.81 for all three methods. The average R^2 value for all three models was 0.66. Again, the similar performance between the three models does not provide any insight into preference for one model and is likely a result of the calibration procedure. Figure 4d shows that the LE_{Rain} model performs well through the entire validation period. Similar to the calibration period, the LE_{Rain} model appears to underestimate the nightly low, which causes the following daily high to be overestimated. Nonetheless, these R^2 values lend confidence to the modeled results as the LE_{Rain} model only performs slightly poorer compared to the calibration period.

Reid and Brock (2010) found R^2 values of 0.94 and 0.52 for temperature sensors at the surface and at a depth of 15 cm, respectively. While the R^2 value of 0.94 is higher than those found in this study, the range of R^2 is comparable. The slightly lower R^2 values in this study may be a result of using meteorological data from an AWS located 14 km away from the glacier. Furthermore, longwave radiation was estimated from remotely sensed data, which may also influence model performance as previously discussed.

TCD
9, 3503–3540, 2015

5.3 Modeled ablation rates

Ablation rates were computed for the 10 sites with temperature sensors, as estimates of their albedo, thermal conductivity, and surface roughness were available from the results of model calibration and validation. The modeled ablation over the entire duration of the study period (02 June to 12 October 2015) varied from 0.30 to 2.04 m among the three methods (Fig. 5). On average the LE_{Zero} model overestimated the LE_{Rain} and $LE_{RH_{100}}$ models by 2.4 and 5.4 %, respectively. The slight variations in ablation between the methods are directly related to the differences in their calibrated parameters. The slightly higher ablation rates for the LE_{Zero} model is likely attributed to the slightly higher values of thermal conductivities and the lack of a latent heat flux term to remove heat from the debris. Figure 5 shows there is a clear relationship between debris thickness and ablation as thin debris promotes ablation while thick debris insulates the ice thereby retarding ablation. The scatter found throughout the curve, specifically between 0.25 and 0.50 m, is due to the site-specific debris properties and the slope and aspect of each site. The modeled ablation of Site 4 shows the ablation curve levels off for thick debris as expected. The ablation estimated at Site 13, which has the smallest value of thermal conductivity (0.47 $W m^{-1} K^{-1}$) is just slightly higher than the ablation at Site 4, despite having a debris thickness of 0.33 m compared to 1.5 m, respectively. This highlights the importance of accurately measuring and modeling the thermal conductivity of the debris.

The modeled ablation rates may also be compared to the measured ablation rates. Specifically, Sites 13 and 15 had measured ablation rates of 0.85 and 0.89 m, respectively, compared to their modeled ablation rates of 0.35 and 1.16 m, respectively, for the LE_{Rain} model. As previously discussed, Site 13 had multiple temperature sensors, which allowed the thermal conductivity to be estimated; however, the R^2 at a depth of 0.20 m was markedly lower than other data at this site. Similarly, the large discrepancy in modeled and measured ablation rates suggests a problem with one or other dataset and is likely attributed to the thermal conductivity. Thermal conductivity could be better

TCD
9, 3503–3540, 2015

resolved by (a) accurately measuring the depth of the temperature sensors during installation and retrieval, if possible, to monitor the movement of sensors during the melt season, (b) installing additional sensors (e.g., 5 cm spacing) that allow any changes in sensor depth to become apparent, and (c) measuring moisture in the debris at various depths.

The difference between the modeled and measured ablation rates at Site 15 may also be a result of the thermal conductivity parameter (1.61 $W m^{-1} K^{-1}$), which is slightly higher than thermal conductivities previously reported in the Khumbu, which ranged from 0.60 to 1.29 $W m^{-1} K^{-1}$. Furthermore, a comparison of the daily average temperatures for Site 15 reveals there was about an hour lag between the modeled and measured temperatures (results not shown). Lags between temperatures are typically a result of their depth (Conway and Rasmussen, 2000), which is apparent in Fig. 4a as the 0.10 m sensor lags behind the 0.01 m sensor. It is likely that debris moved over the melt season causing the measured temperature to be at a lower depth than 0.01 m, which would greatly influence the model calibration and potentially cause the thermal conductivity to vary. Site 5 was the only other site where a slight lag was observed between the measured and modeled temperatures. The modeled ablation was 0.81 m using the LE_{Rain} model, while the ablation stake melted completely out of the ice indicating greater than 1 m of ablation. All the other model estimates of ablation were near to or greater than 1 m, agreeing well with the ablation stakes at their sites, which completely melted out of the ice.

The ablation results also show strong seasonal trends with maximum melt rates occurring in June, July, and August. These ablation rates appear to taper off towards the transition seasons. Melt rates in July and August ranged from 0.3–1.7 cm day^{-1} based on the debris thickness, which is consistent with empirical relationships between mean daily ablation rate and debris thickness found on other glaciers (Nicholson and Benn, 2006). The total ablation rates are also similar to those measured on Imja-Lhotse Shar glacier using multiple DEMs, which were 1.45 ± 0.52 m yr^{-1} (Bolch et al., 2011), thereby lending confidence to the results.

TCD
9, 3503–3540, 2015

5.4 Sensitivity analysis

A sensitivity analysis was performed to assess how albedo, thermal conductivity, and surface roughness affect the total ablation (Table 4). The total ablation using the LE_{Rain} model was used as the baseline case and each parameter was varied by ±10 %. Table 4 shows that the total ablation is most sensitive to changes in thermal conductivity with a ±10 % change resulting in an average ±8.2 % change in total melt. Total ablation is also moderately sensitive to albedo as a ±10 % change corresponded to an average ±3.6 % change in total melt. Lastly, the surface roughness appeared to have the least amount of influence on total melt with a ±10 % resulting in an average ±1.5 % change in total ablation.

It is important to note that Table 4 expresses relative changes in percentages to highlight the sensitivity of total melt with respect to each parameter. Therefore, the change in total melt is highly variable for each site, e.g., a ±10 % in thermal conductivity causes the total melt to change by ±0.04 m for Site 4 compared to a change of ±0.14 m for Site 20. This suggests it is increasingly important to accurately measure these parameters for sites with higher amounts of ablation, i.e., typically sites with thinner debris. Furthermore, the 10 % variation was used to standardize the impact of each parameter; however, actual variations in the field may be greater than 10 %. For example, Site 6 visually appeared to have grain sizes similar to Site A (0.007 m), yet the model optimization yielded a surface roughness value of 0.030 m. This variation is much greater than 10 % and highlights the importance of measuring these parameters.

5.5 Temporal resolution

Nicholson and Benn (2006) proposed that the temperature gradient in the debris may be assumed to be linear at a time step greater than a day, but is nonlinear for shorter time steps. This would have important implications for modeling melt on remote debris-covered glaciers where meteorological data is not available and reanalysis datasets could be used instead. The importance of temporal resolution was analyzed using 6 h

TCD
9, 3503–3540, 2015

and daily average data from Pyramid Station, which are consistent with the temporal resolution of NCEP/NCAR reanalysis datasets. To be consistent with this reanalysis dataset such that only the effects of temporal resolution were analyzed, the wind speed and relative humidity used were instantaneous values from Pyramid Station, while all the other variables were 6 h averages. For the daily time step, all the parameters were daily averages and the temperature profile in the debris is assumed to be linear. The LE_{Rain} model was used to model the latent heat flux.

The R^2 correlation coefficients and total melt at each site were assessed to determine the effects of temporal resolution. The R^2 using the 6 h data ranged from 0.24 to 0.85 with an average value of 0.53. Figure 6a shows the surface temperature at Site 11 does fairly well (R^2 = 0.62) at modeling the measured surface temperatures over the calibration period. The lower R^2 values compared to the 30 min time step appears to be a result of the 6 h model underestimating the daily high, which occurs around 15:00 LT (local time) each day. Furthermore, Fig. 6b shows the 6 h model poorly replicates the measured data towards the transition seasons when snowfall becomes significant. Snowfall is problematic in the model for large time steps because the model assumes the snow is on the surface for the entire time step. Therefore, a small snow event that could melt quickly on the debris and then allow the debris to warm up during the day is perceived to remain on the snow for the 6 h time step. The same problem arises at the daily time step, so a snow-free model was used instead (Fig. 6c).

Since we are most interested in understanding the effects of temporal resolution here, the 6 h data and daily averages from 02 June to 25 September 2014 were assessed, which is prior to the time when snowfall was recorded each day. A comparison of all the modeled and measured temperatures reveals the 6 h model underestimates the measured temperatures by an average of 3.4 (±3.9) K. Comparison of the total ablation through 25 September reveals the total ablation is consistently underestimated at all sites by an average of 17 (±6) %. The lower estimate of ablation is likely a result of the underestimation of the daily high as previous discussed. Similarly, the daily time step also slightly underestimates the measured temperature on average by 0.3

TCD
9, 3503–3540, 2015

(±2.3) K. The total ablation is also underestimated by an average of 9 (±9) % with one site overestimating the melt. These results suggest that if high-temporal meteorological data are not available, it may be feasible to use 6 h data or daily averages to estimate ablation over the melt season; however, the model will perform poorly towards the transition season when snow falls and the ablation will likely be slightly underestimated.

6 Conclusions

Debris thickness greatly impacts ablation rates on debris-covered glaciers; however, incorporating debris cover into energy balance models is still hampered by a lack of knowledge of the debris properties. Fieldwork performed on Imja-Lhotse Shar glacier over the 2014 melt season was used to develop new techniques to measure surface roughness, which yielded realistic values for various grain sizes. Temperature sensors and ablation stakes installed in the debris were also used to assess the performance of a debris-covered energy balance model using three different methods for estimating the latent heat flux. All three models performed well, as a result of the calibration procedure, which allowed variations in the lack of latent heat flux to be compensated for by adjusting the debris properties. However, the LE_{Rain} and $LE_{RH_{100}}$ models yielded more reasonable values of latent heat fluxes and performed slightly better. This suggests that in a data-scarce region either the LE_{Rain} or $LE_{RH_{100}}$ model may be used if relative humidity or precipitation data are available.

A sensitivity analysis revealed ablation rates were most sensitive to variations in thermal conductivity, followed by albedo and surface roughness. This highlights the importance of measuring the thermal conductivity and the moisture content in the debris. The effect of temporal resolution on model performance was also explored using a 6 h time step and a daily time step. The 6 h time step was found to underestimate the daily high each day, which caused the ablation rates to also be slightly underestimated. The daily time step typically underestimated measured temperatures and ablation rates as well.

TCD
9, 3503–3540, 2015

Future studies should continue to work on incorporating the water content in the debris into debris-covered energy balance models and determine its effect on thermal conductivity (Collier et al., 2014). Furthermore, an increased understanding of how the albedo may vary over the course of the day, the course of the melt season, and as a function of debris saturation, may significantly improve model performance. Despite the model being least sensitive to changes in surface roughness, the surface roughness will still significantly impact modeled turbulent heat fluxes. The methods developed in this study have the potential to be scaled up such that maps of surface roughness on a whole glacier scale may be developed in the future.

Acknowledgements. The authors acknowledge the support of the USAID Climate Change Resilient Development (CCRD) project for the support of Rounce. The meteorological data from Pyramid Station used in this study was collected within the SHARE Project thanks to contributions from the Italian National Research Council and the Italian Ministry of Foreign Affairs. The NCEP Reanalysis data provided by the NOAA/OAR/ESRL PSD, Boulder, Colorado USA from their website http://www.esrl.noaa.gov/psd/ was also very helpful. We also acknowledge the support of Dhananjay Regmi of Himalayan Research Expeditions for temperature sensors and logistical support during fieldwork.

References

Benn, D. I., Bolch, T., Hands, K., Gulley, J., Luckman, A., Nicholson, L. I., Quincey, D., Thompson, S., Toumi, R., and Wiseman, S.: Response of debris-covered glaciers in the Mount Everest region to recent warming, and implications for outburst flood hazards, Earth-Sci. Rev., 114, 156–174, 2012.

Bolch, T., Pieczonka, T., and Benn, D. I.: Multi-decadal mass loss of glaciers in the Everest area (Nepal Himalaya) derived from stereo imagery, The Cryosphere, 5, 349–358, doi:10.5194/tc-5-349-2011, 2011.

Brock, B. W., Willis, I. C., and Sharp, M. J.: Measurement and parameterization of aerodynamic roughness length variations at Haut Glacier d'Arolla, Switzerland, J. Glaciol., 52, 281–297, 2006.

TCD
9, 3503–3540, 2015

Brock, B. W., Mihalcea, C., Kirkbride, M. P., Diolaiuti, G., Cutler, M. E. J., and Smiraglia, C.: Meteorology and surface energy fluxes in the 2005–2007 ablation seasons at the Miage debris-covered glacier, Mont Blanc Massif, Italian Alps, J. Geophys. Res., 115, D09106, doi:10.1029/2009JD013224, 2010.

Collier, E., Nicholson, L. I., Brock, B. W., Maussion, F., Essery, R., and Bush, A. B. G.: Representing moisture fluxes and phase changes in glacier debris cover using a reservoir approach, The Cryosphere, 8, 1429–1444, doi:10.5194/tc-8-1429-2014, 2014.

Conway, H. and Rasmussen, L. A.: Summer temperature profiles within supraglacial debris on Khumbu Glacier, Nepal, Debris-Covered Glaciers, in: Proceedings of a workshop held at Seattle, September 2000, Washington, USA, 2000.

Foster, L. A., Brock, B. W., Cutler, M. E. J., and Diotri, F.: Instruments and methods: a physically based method for estimating supraglacial debris thickness from thermal band remote-sensing data, J. Glaciol., 58, 677–691, doi:10.3189/2012JoG11J194, 2012.

Fujita, K. and Sakai, A.: Modelling runoff from a Himalayan debris-covered glacier, Hydrol. Earth Syst. Sci., 18, 2679–2694, doi:10.5194/hess-18-2679-2014, 2014.

Fyffe, C. L., Reid, T. D., Brock, B. W., Kirkbride, M. P., Diolaiuti, G., Smiraglia, C., and Diotri, F.: A distributed energy-balance melt model of an alpine debris-covered glacier, J. Glaciol., 60, 587–602, doi:10.3189/2014JoG13J148, 2014.

Inoue, J. and Yoshida, M.: Ablation and heat exchange over the Khumbu Glacier, Seppyo, J. Japan. Soc. Snow Ice, 41, 26–31, 1980.

Kalnay, E., Kanamitsu, M., Kistler, R., Collins, W., Deaven, D., Gandin, L., Iredell, M., Saha, S., White, G., Woollen, J., Zhu, Y., Chelliah, M., Ebisuzaki, W., Higgins, W., Janowiak, J., Mo, K. C., Ropelewski, C., Wang, J., Leetmaa, A., Reynolds, R., Jenna, R., and Dennis, J.: The NCEP/NCAR 40-year reanalysis project, B. Am. Meteorol. Soc., 77, 437–470, 1996.

Kayastha, R. B., Takeuchi, Y., Nakawo, M., and Ageta, Y.: Practical prediction of ice melting beneath various thickness of debris cover on Khumbu Glacier, Nepal, using a positive degree-day factor, Int. Assoc. Hydrol. Sci. Publ., 264, 71–81, 2000.

Lejeune, Y., Bertrand, J., Wagnon, P., and Morin, S.: A physically based model of the year-round surface energy and mass balance of debris-covered glaciers, J. Glaciol., 49, 327–344, doi:10.3189/2013JoG12J149, 2013.

Lettau, H.: Note on aerodynamic roughness-parameter estimation on the basis of roughness-element description, J. Appl. Meteorol., 8, 828–832, 1969.

TCD
9, 3503–3540, 2015

Munro, D. S.: Surface roughness and bulk heat transfer on a glacier: comparison with eddy correlation, J. Glaciol., 35, 343–348, 1989.
Nakawo, M. and Young, G. J.: Field experiments to determine the effect of a debris layer on ablation of glacier ice, Ann. Glaciol., 2, 85–91, 1981.
Nicholson, L. and Benn, D. I.: Calculating ice melt beneath a debris layer using meteorological data, J. Glaciol., 52, 463–470, 2006.
Nicholson, L. and Benn, D. I.: Properties of natural supraglacial debris in relation to modelling sub-debris ice ablation, Earth Surf. Proc. Land., 38, 490–501, doi:10.1002/esp.3299, 2012.
Østrem, G.: Ice Melting under a thin layer of moraine, and the existence of ice cores in moraine ridges, Geografiska Annaler, 41, 228–230, 1959.
Rees, W. G. and Arnold, N. S.: Scale-dependent roughness of a glacier surface: implications for radar backscatter and aerodynamic roughness modelling, J. Glaciol., 52, 214–222, 2006.
Reid, T. D. and Brock, B. W.: An energy-balance model for debris-covered glaciers including heat conduction through the debris layer, J. Glaciol., 56, 903–916, 2010.
Reid, T. D., Carenzo, M., Pellicciotti, F., and Brock, B. W.: Including debris cover effects in a distributed model of glacier ablation, J. Geophys. Res., 117, D18105, doi:10.1029/2012JD017795, 2012.
Rounce, D. R. and McKinney, D. C.: Debris thickness of glaciers in the Everest area (Nepal Himalaya) derived from satellite imagery using a nonlinear energy balance model, The Cryosphere, 8, 1317–1329, doi:10.5194/tc-8-1317-2014, 2014.
Snavely, N.: Scene Reconstruction and Visualization From Internet Photo Collections, unpublished PhD thesis, University of Washington, USA, 2008.
Snavely, N., Seitz, S. M., and Szeliski, R.: Modeling the world from internet photo collections, Int. J. Comput. Vision, 80, 189–210, doi:10.1007/s11263-007-0107-3, 2008.
Sturm, M., Holmgren, J., König, M., and Morris, K.: The thermal conductivity of seasonal snow, J. Glaciol., 43, 26–41, 1997.
Sturm, M., Perovich, D. K., and Holmgren, J.: Thermal conductivity and heat transfer through the snow on the ice of the Beaufort Sea, J. Geophys. Res., 107, 8043, doi:10.1029/2000JC000409, 2002.
Szeliski, R.: Computer Vision: Algorithms and Applications, Springer, London, 2011.
Takeuchi, Y., Kayastha, R. B., and Nakawo, M.: Characteristics of ablation and heat balance in debris-free and debris-covered areas on Khumbu Glacier, Nepal Himalayas, in the premonsoon season, Int. Assoc. Hydrol. Sci. Publ., 264, 53–61, 2000.

TCD
9, 3503–3540, 2015

Westoby, M. J., Brasington, J., Glasser, N. F., Hambrey, M. J., and Reynolds, J. M.: "Structure-from-Motion" Photogrammetry: a low-cost, effective tool for geoscience applications, Geomorphology, 179, 300–314, 2012.

Zhang, Y., Fujita, K., Liu, S., Liu, Q., and Nuimura, T.: Distribution of debris thickness and its effect on ice melt at Hailuogou Glacier, Southeastern Tibetan Plateau, using in situ surveys and ASTER imagery, J. Glaciol., 57, 1147–1157, 2011.

TCD
9, 3503–3540, 2015

Table 1. Details of the debris thickness, topography, and monitoring equipment installed at each site. Bold notes an estimation of debris thickness. T_s denotes surface temperature.

Site	Debris thickness (m)	Slope (°)	Aspect (°)	Temperature sensor depth (m)	Ablation stake	z_0 photos
4	**1.50**	17	232	T_s, 0.10, 0.20, 0.40, 0.83	–	–
5	0.54	24	158	T_s	x	–
6	0.08	37	237	T_s	x	–
7	0.52	31	65	–	x	–
8	0.20	32	187	–	x	–
10	0.07	32	337	–	x	–
11	0.45	32	197	T_s, 0.05, 0.10, 0.20, 0.36	x	–
12	0.15	19	265	–	x	–
13	0.33	29	295	T_s, 0.05, 0.10, 0.20	x	–
14	0.26	23	148	T_s, 0.05, 0.24	x	–
15	0.37	29	40	T_s	x	–
16	0.15	32	264	–	x	–
17	0.27	29	228	T_s	x	–
19	0.37	33	198	T_s	x	–
20	0.20	29	200	T_s	x	–
A	–	–	–	–	–	x
B	–	–	–	–	–	x
C	–	–	–	–	–	x
D	–	–	–	–	–	x

TCD
9, 3503–3540, 2015

Table 2. Errors associated with the DEM and summary of z_0 values for each site.

Site	DEM Error (m)				z_0 (m)			
	x	*y*	*z*	Total	Mean	SD	Min	Max
A	0.015	0.018	0.007	0.024	0.011	0.004	0.002	0.030
B	0.004	0.007	0.001	0.008	0.030	0.023	0.005	0.165
C	0.010	0.007	0.002	0.012	0.007	0.005	3×10^{-4}	0.039
D	0.006	0.007	0.001	0.009	0.011	0.009	0.001	0.075

TCD
9, 3503–3540, 2015

Table 3. Optimized values of albedo, thermal conductivity, and surface roughness for three methods of estimating latent heat flux over the calibration period.

Site	LE_{Rain}			$LE_{RH_{100}}$			LE_{Dry}		
	α	k^1	z_0^2	α	k^1	z_0^2	α	k^1	z_0^2
4	0.12	1.44	0.018	0.10	1.44	0.022	0.10	1.44	0.026
5	0.40	1.62	0.014	0.40	1.62	0.016	0.40	1.62	0.017
6	0.40	1.15	0.030	0.40	1.15	0.030	0.40	1.34	0.030
11	0.26	1.62	0.015	0.20	1.62	0.022	0.24	1.62	0.022
13	0.14	0.47	0.030	0.18	0.47	0.028	0.19	0.47	0.030
14	0.39	1.62	0.017	0.37	1.62	0.022	0.38	1.62	0.022
15	0.34	1.61	0.007	0.36	1.62	0.007	0.37	1.62	0.007
17	0.29	1.62	0.007	0.28	1.62	0.007	0.29	1.62	0.007
19	0.33	1.62	0.019	0.28	1.62	0.028	0.30	1.62	0.028
20	0.27	1.62	0.007	0.27	1.62	0.007	0.29	1.62	0.007
Avg	0.29	1.36	0.019	0.29	1.36	0.021	0.30	1.39	0.022
SD	0.12	0.43	0.008	0.12	0.43	0.008	0.12	0.42	0.008

[1] units of $W m^{-1} K^{-1}$; [2] units of m.

TCD
9, 3503–3540, 2015

Table 4. Sensitivity analysis showing percent changes relative to the total ablation (m) as a function of calibrated parameters (α, k, z_0) for all sites over the study period using the LE_{Rain} model as the baseline case.

		Site									
		4	5	6	11	13	14	15	17	19	20
Baseline ablation (m)		0.33	0.81	1.82	0.98	0.35	1.41	1.16	1.46	0.99	1.95
Parameter	Adjustment	% Change									
α	+10 %	−1.2	−5.5	−4.6	−2.9	−1.3	−5.1	−4.3	−3.5	−4.0	−3.1
	−10 %	+1.2	+5.6	+4.5	+3.1	+1.2	+5.0	+4.4	+3.4	+3.9	+3.2
k	+10 %	+11.2	+8.5	+6.5	+8.5	+9.4	+7.3	+7.4	+7.1	+8.1	+6.6
	−10 %	−11.1	−8.8	−6.7	−8.6	−9.6	−7.7	−7.8	−7.6	−8.5	−7.0
z_0	+10 %	−2.1	−1.6	−1.0	−1.6	−2.1	−1.3	−1.2	−1.3	−1.6	−1.0
	−10 %	+2.4	+1.6	+1.1	+1.8	+2.3	+1.4	+1.2	+1.2	+1.7	+1.2

TCD
9, 3503–3540, 2015

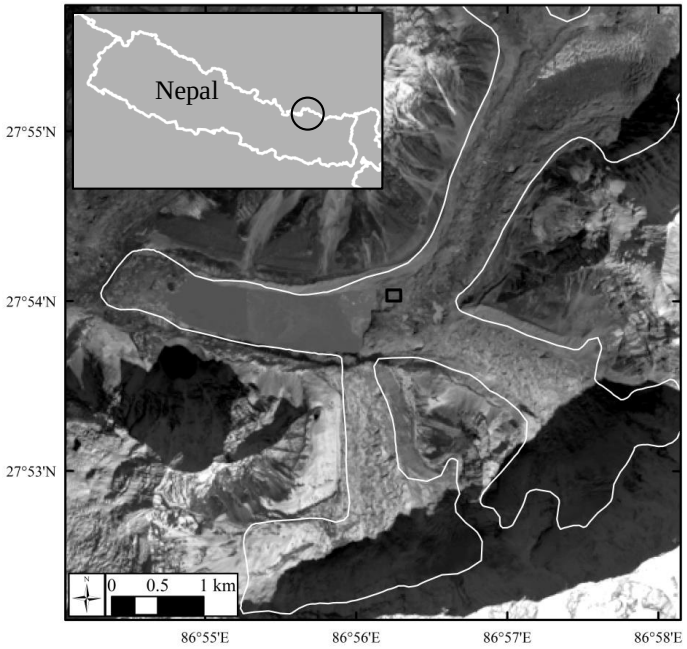

Figure 1. Imja-Lhotse Shar glacier with the focus area of this study highlighted by the rectangular box several kilometres up-glacier from the terminus, and the site location within Nepal shown in the inset.

TCD
9, 3503–3540, 2015

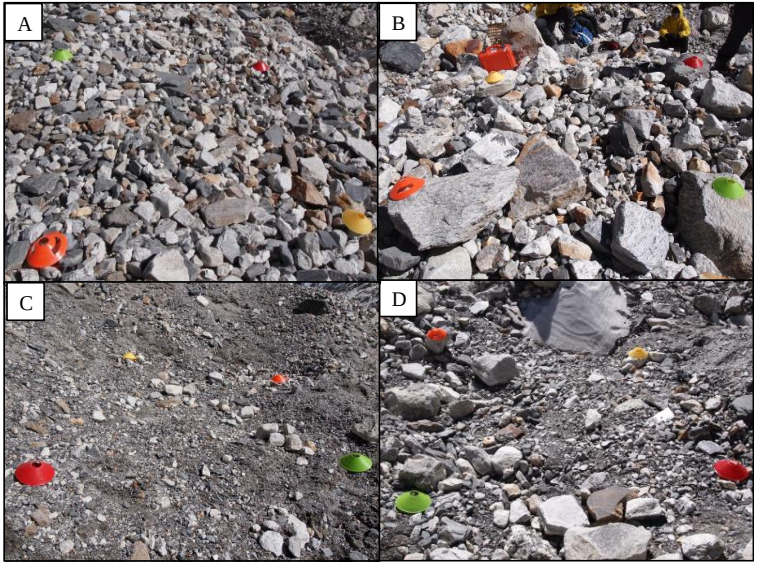

Figure 2. Sites A–D highlighting the variations in grain sizes that are found over the debris-covered portion of Imja-Lhotse Shar glacier.

TCD
9, 3503–3540, 2015

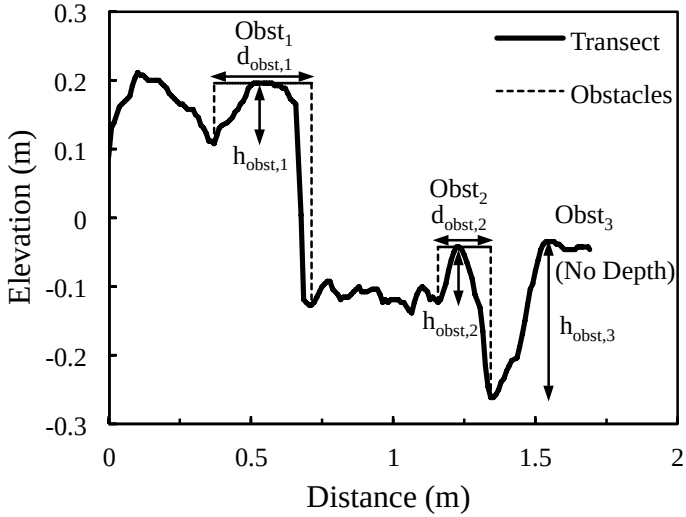

Figure 3. Transect from Left-Right of Site B showing the identification of obstacles (Obst) and their corresponding heights (h_{obst}) and depths (d_{obst}).

TCD
9, 3503–3540, 2015

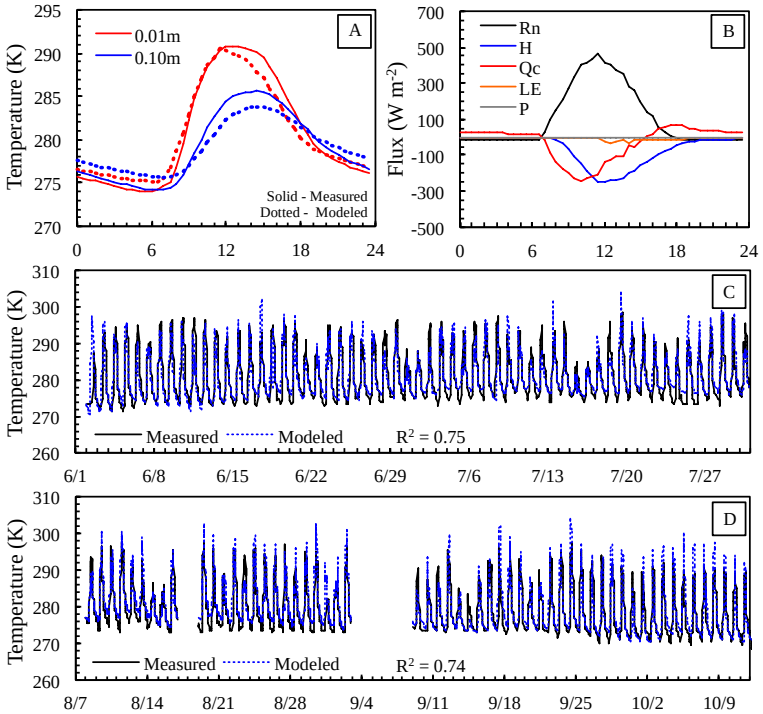

Figure 4. Various plots for Site 11 using the LE_{Rain} model showing **(a)** average daily temperatures at two depths (solid and dashed lines indicate measured and modeled temperatures, respectively), **(b)** average daily energy fluxes, **(c)** measured and modeled temperatures at a depth of 0.01 m over the calibration period, and **(d)** measured and modeled temperatures over the validation period.

TCD
9, 3503–3540, 2015

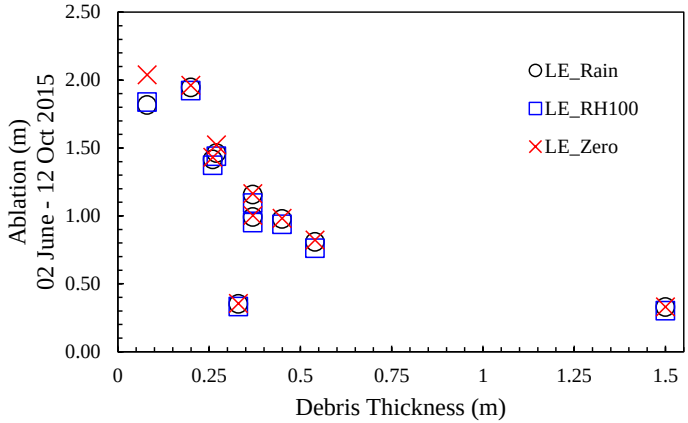

Figure 5. Modeled ablation with respect to debris thickness for all 10 sites from 02 June to 12 October 2015 for each of the three methods used to model the latent heat flux.

TCD
9, 3503–3540, 2015

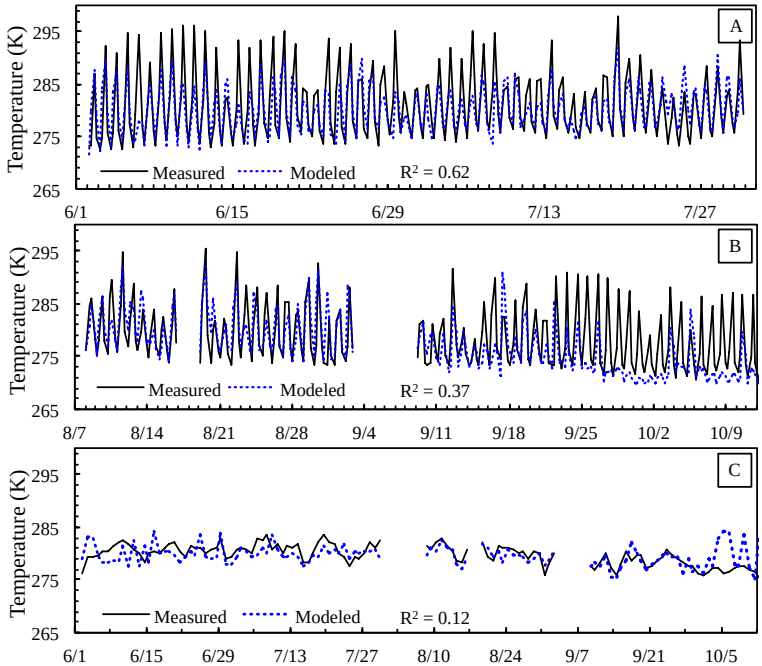

Figure 6. Modeled and measured surface temperature at Site 11 over the **(a)** calibration period and **(b)** validation period using 6 h data, and **(c)** entire period using daily averages.

TCD
9, 3503–3540, 2015